High Dynamic Performance Nonlinear Source Emulator

Nguyen-Duy, Khiem; Knott, Arnold; Andersen, Michael A. E.

Published in:
IEEE Transactions on Power Electronics

Link to article, DOI:
10.1109/TPEL.2015.2437880

Publication date:
2016

Document Version
Peer reviewed version

High Dynamic Performance Nonlinear Source Emulator

Khiem Nguyen-Duy, *Student Member, IEEE*, Arnold Knott, *Member, IEEE*, and Michael A. E. Andersen, *Member, IEEE*

***Abstract*—As research and development of renewable and clean energy based systems is advancing rapidly, the nonlinear source emulator (NSE) is becoming very essential for testing of maximum power point trackers or downstream converters. Renewable and clean energy sources play important roles in both terrestrial and nonterrestrial applications. However, most existing NSEs have only been concerned with simulating energy sources in terrestrial applications, which may not be fast enough for testing of nonterrestrial applications. In this paper, a high-bandwidth NSE is developed that is able to simulate the behaviors of a typical nonlinear source under different critical conditions that can happen during their operations. The proposed 200-W NSE, which consists of a fourth-order output filter buck converter and a novel nonlinear small-signal reference generator, can quickly react not only to an instantaneous change in the input source but also to a load step between nominal and open circuit. Moreover, all of these operation modes have a very fast settling time of only 10 μs, which is hundreds of times faster than that of existing works. This attribute allows for higher speed and a more efficient maximum power point tracking algorithm. The proposed NSE, therefore, offers a superior dynamic performance among devices of the same kind.**

***Index Terms*—Current–voltage characteristics, dc–dc power converters, energy resources, nonlinear circuits, renewable energy sources.**

I. Introduction

A. Background

THE world is rapidly changing from using fossil based energy, which is facing exhaustion, to the use of renewable and clean energy sources, such as wind, sun, fuel cell energy, and battery power. In the testing and development phase of these energy sources, the use of nonlinear source emulators (NSEs) offers many advantages over the use of their real counterparts. First, NSEs are compact and do not require as large of a testing space as nonlinear sources such as wind turbines or PV panels. Second, the cost of a test system using NSEs is usually less than that of actual nonlinear sources [1]. Another example is that of nonrechargeable power batteries, which would have to be disposed of after each test; hence, testing would be expensive and extra care must be taken to not harm the environment [2], [3]. On the contrary, a battery emulator constructed from a power electronics converter can be reused for a long time and is not only cost effective but also friendly to the environment [4]–[8]. Finally, an NSE offers flexible and reproducible test conditions through their programmable set points. On the other hand, testing conditions of a real nonlinear source such as a PV or wind energy source are very difficult to be reproduced because of their dependence on weather, season, coverage, and time of the day of testing. With the many possible advantages that it can offer, the NSE has become an important and beneficial element in testing of power conditioning units. As a result, research on the development of NSEs has received great attention [2]–[13].

Manuscript received December 5, 2014; revised March 17, 2015; accepted May 8, 2015. Date of publication June 1, 2015; date of current version November 16, 2015. This work was supported by the Danish Innovationsfonden (in English: Innovation Fund Denmark) under Grant 045-2010-3 that provided this research opportunity.

K. Nguyen-Duy is with SSBV-Rovsing, 2740 Skovlunde, Denmark (e-mail: knduy1@gmail.com).

A. Knott and M. A. E. Andersen are with the Department of Electrical Engineering, Technical University of Denmark, 2800 Kgs. Lyngby, Denmark (e-mail: akn@elektro.dtu.dk; ma@elektro.dtu.dk).

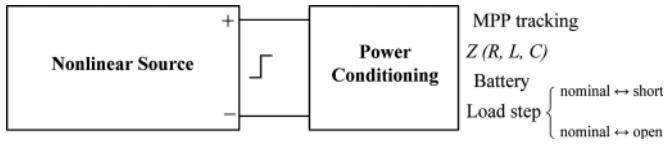

Fig. 1. Connection between a nonlinear source and a power conditioning unit.

A power conditioning unit that connects with a nonlinear source can take many different forms, which can be seen in Fig. 1. It can be a maximum power point (MPP) tracker that tracks the MPP of the nonlinear source. It can also be an impedance such as an ohmic load, an inductive load, or a capacitive load. In addition, a power conditioning unit can also be a power battery that stores energy from the nonlinear source. It can also be a system that regulates average output voltage by applying a frequent load step between nominal load and short circuit, or a load step between nominal load and open circuit. In voltage regulation by means of load stepping, the system is pulse width modulated and switching with high frequency (20 kHz or more [14]). The two different types of load step will be presented in more detail later in the next section.

The static voltage–current relationship of a fuel cell system can be represented by a high-order polynomial as in [11], [12]

$$V = f(I) = \alpha_3 I^3 + \alpha_2 I^2 + \alpha_1 I + \alpha_0 \tag{1}$$

where V is the fuel cell terminal voltage, I is the fuel cell output current, and α_0–α_3 are the coefficients of the static *V–I* curve; they change according to the change of hydrogen concentration. Fig. 2 shows an example of the static *V–I* curve characteristics of a fuel cell system at different hydrogen concentration levels. With each hydrogen concentration level of a specific fuel cell system, there exists a set of four coefficients α_0–α_3 derived by

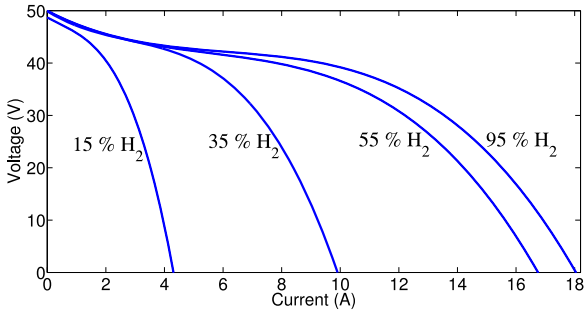

Fig. 2. Changes of dc operating point due to changes of hydrogen concentration levels in a fuel cell system [11], [12].

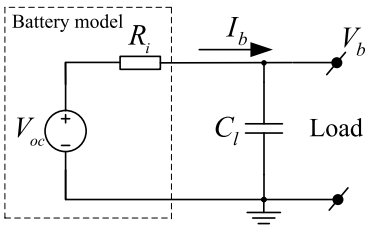

Fig. 3. Circuit model of a battery with load [2].

means of curve fitting that can describe the system steady-state *V–I* curve.

There has not been any satisfactory equivalent electrical circuit developed that can closely describe the *V–I* relationship of a hydrogen fuel cell system because of its high nonlinearity. This is one of the reasons why nonlinear *V–I* reference curves in existing fuel cell emulators have always been implemented by digital control circuits such as digital signal processor and field-programmable gate array (FPGA), in order to take advantage of their mathematical processing power [9]–[13].

Batteries are used extensively in industry such as in electric vehicle and hybrid electric vehicle applications [2], [3], [7]. A circuit model of a battery is shown in Fig. 3. The dashed-line box models a battery, in which $V_{\rm oc}$ and R_i are the open-circuit voltage and internal resistance, respectively. The rest of the circuit models an output with a filter capacitance C_l [2], [3]. The available voltage at the output of the battery is simply

$$V_b = V_{\rm oc} - IR_i. \tag{2}$$

During the discharge of the battery, $V_{\rm oc}$ decreases while R_i increases; both of them are dependent on the state of the battery and its internal temperature.

In the modeling of a PV panel, the *five-parameter model* [15], [16] is widely used to describe its electrical characteristic. The model is shown in Fig. 4. It is also called the *single-diode model* [15]–[17]. The current is related to the terminal voltage $V_{\rm PV}$ and the short-circuit current $I_{\rm SC}$ by

$$I_{\rm PV} = I_{\rm SC} - I_o(\mathrm{e}^{(\frac{V_{\rm PV}+I_{\rm PV}R_S}{n\,V_t})} - 1) - \frac{V_{\rm PV}+I_{\rm PV}R_S}{R_P}. \tag{3}$$

In this model, R_P is the *parallel resistor* that models the loss due to manufacturing defects. R_S is the *series resistor* that

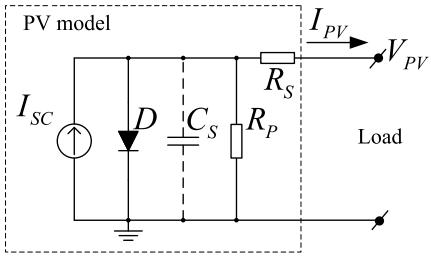

Fig. 4. Five-parameter model of a PV panel.

models the loss due to mainly three causes: the movement of current through the emitter and base of the PV cell, the contact resistance between the metal contact and the silicon, and the resistance of the top and rear metal contacts [18]. I_o is the *dark saturation current* of the diode, which is the diode leakage current density in the absence of light. V_t is the *thermal voltage*, which is equal to approximately 25.85 mV at a temperature of 300 K. Parameter n is the *ideality factor*—a constant between 1 and 2 that depends on the manufacturing of the PV cell and may slightly vary with the operating point of it. For a given PV cell, the short-circuit current $I_{\rm SC}$ is mainly determined by the intensity of the incident solar radiation, and the open-circuit voltage $V_{\rm OC}$ is mainly determined by the cell temperature.

B. Dynamic Performance of Nonlinear Sources

The hydrogen concentration changes in fuel cell have quite a large time constant. According to [11] and [12], this time constant is 10 s. In other words, it will take approximately 10 s for the voltage and current of a fuel cell to reach its steady state under a change of hydrogen concentration performed by the fuel cell control system.

Furthermore, fuel cell systems have also quite a slow dynamic with regard to load changes [13]. Also according to [11] and [12], the output impedance of a typical fuel cell system has a dominant pole at 20 Hz, which makes the output to react in the range of 50 ms or longer.

In short, fuel cell systems are rather slow systems. As a result, most of the challenges with developing a fuel cell emulator will lie on the digital control unit that calculates the nonlinear reference. On the other hand, from a control point of view, the power converter unit of a fuel cell emulator, which generates power, will not be much of a challenge due to its slow dynamic. It can be easily constructed by programmable off-the-shelf power supplies, such as the work in [11]–[13].

Among the aforementioned nonlinear sources, a PV system is the one that has the most critical demand for transient response. It is, therefore, the focus of this paper to develop a fast response NSE that will be able to emulate the most speed-demanding system among the known nonlinear sources. Since it can emulate the fastest system, it will be capable of simulating any other types of nonlinear source after proper adjustments.

The five-parameter model is sufficient as long as the dynamic performance of a PV panel is not of critical concern. This is the case with existing PV emulators that are designed for

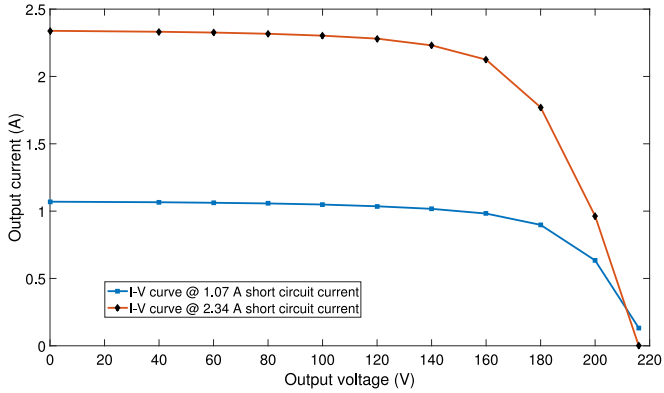

Fig. 5. *I–V* curve generated from measurement data in [20].

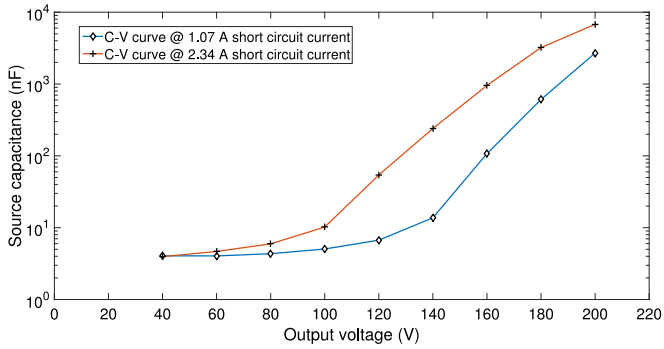

Fig. 6. *C–V* curve generated from measurement data in [20] .

terrestrial applications, where most of the time the main focus is paid to the tracking of the MPP. In fact, the MPP changes with a rather slow speed. According to the survey conducted in [19], existing MPP tracking techniques in the literature have a moderate convergence speed of tens of milliseconds. That implies a requirement for the transient speed of the real PV panel or the PV emulator of approximately 10–100 Hz. In fact, a nonlinear source can experience a frequent load step in some specific operation mode. This is where the dynamic response of a nonlinear source is exceptionally important. This is also where the model in Fig. 4 should take into account the PV panel's intrinsic source capacitance that is shown in dotted lines.

In practice, a real PV panel physically contains an intrinsic source capacitance due to the diffusion capacitance of each PV cell [20]. This capacitance is in parallel with the diode and the parallel resistor. The value of this capacitor varies with operating points of the PV panel. For example, existing work such as [20] reported that the value range of the source capacitance of a 312-W, 400 $\times$ 8 cm^2 silicon PV panel is from approximately 4 nF at the point close to the short circuit, to 6.7 μF at the open circuit. The data reported in [20] are plotted in Figs. 5 and 6.

The presence of the source capacitance plays a critical role in the determination of a PV panel's dynamic response. It makes the output current and voltage of a real PV panel under a load step to undergo a transient time in the range of tens of microseconds to settle down [14]. It is the time for the current source

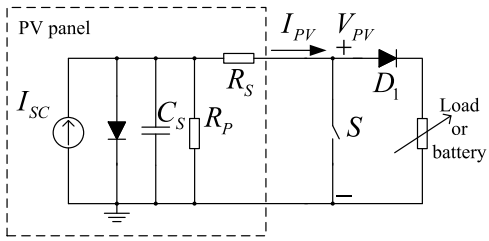

Fig. 7. Circuit configuration of a load step between nominal and short circuit.

$I_{\rm SC}$ to charge the source capacitor C_S until the new operating voltage is reached. This can be verified by the following estimation. Supposing the converter is experiencing a load step, the operating point is moving from the short circuit to a resistive load that corresponds to the operating point of (V_o, I_o)= (160 V, 0.982 A), where the short-circuit current is 1.07 A. Thus, $R = V_o/I_o = 163\ \Omega$. From Fig. 6, the source capacitance is $C_S = 107$ nF. Considering a current source of $I_{\rm SC} = 1.07$ A constantly supplies a load that consists of a source capacitance C_S of 107 nF in parallel with a resistive load R of 163 Ω, the output voltage as a function of time is

$$v_o(t) = I_{\rm SC} R(1 - {\rm e}^{\frac{-t}{RC_S}}). \tag{4}$$

The transient time for this PV system to move from short circuit $(0, I_{\rm SC})$ to (V_o, I_o) is approximated by

$$\Delta t = -RC_S \ln\left(1 - \frac{V_o}{I_{\rm SC} R}\right) = 4.37 \times 10^{-5}{\rm s} = 43.7\ \mu{\rm s}. \tag{5}$$

By the same approximation method, it will take approximately 1.1 μs for this PV system to complete the transition from the short circuit to the operating point (V_2, I_2)= (60 V, 1.062 A). In summary, it is proven that it will take the PV panel only microseconds to tens of microseconds to finish a transient. Notice that this dynamic is thousands of times faster than the dynamic of a typical fuel cell system, which is stated above to be in the range of tens of milliseconds to a few seconds.

Moreover, much more extreme conditions are usually met in nonterrestrial applications (such as PV panels attached to sky explorers) than those in terrestrial applications. First, a PV panel can experience a step change of input source or, i.e., irradiation, during the period when sunlight is obscured by the Earth or the Moon. This step change of input source can happen right at the time when the sky explorer either enters or leaves the shadow. Second, specific system operation modes, namely the frequent load step between nominal and short circuit [14], [21]–[28] and the load step between nominal and open circuit, are usually adopted in nonterrestrial applications. These modes demand for much faster dynamic responses than those in terrestrial applications. The circuit configuration of these two operation modes (charging modes) is illustrated in Figs. 7 and 8. In these figures, C_S is the source capacitance, S is a switch, and D_1 is a blocking diode to prevent the load or battery to be shorted when S is turned ON. A battery is the essential source of energy for sky explorers during night time when sunlight is absent. In the load

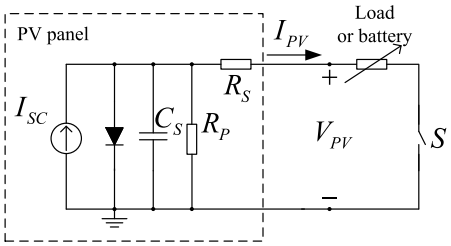

Fig. 8. Circuit configuration of a load step between nominal and open circuit.

step between nominal and short circuit, the circuit is switching between the short-circuit point to the operating point determined by the load applied. In the load step between nominal and open circuit, namely the series switching regulation, a load step is performed between the open-circuit condition and the nominal load. The switching frequency of switch S in these tests is, for example, typically 20 kHz such as discussed in [14], but it can be increased to hundreds of kilohertz. Under these operation modes, the dynamic behavior of the PV panel is significantly important. An ideal PV panel without any capacitance will react immediately without any delay; the transition from one operating point to the other is instantaneous. With the effect of the source capacitor, a practical PV panel under these conditions will react within tens of microseconds, which has been proven in (5).

Because test conditions in terrestrial applications are less extreme compared to those in nonterrestrial applications, a PV emulator designed for terrestrial applications might not be fast enough for testing of nonterrestrial applications. Let us review the performance of existing PV emulators in the next section.

C. Dynamic Performance of Existing PV Emulators

Researchers have proposed different NSEs. They can be classified into the three following categories. The first category is voltage-controlled approach. This is where the power circuit is a voltage-controlled amplifier. The output current is sensed and fed to a reference generator. The reference generator produces a reference output-voltage signal for the power circuit to amplify [1], [29]–[37].

The second category is current-controlled approach, where the power circuit is a current-controlled amplifier. The output voltage is sensed and fed to a reference generator. The reference generator produces a reference output-current signal for the power circuit to amplify [38], [39].

The third category is when both a current-controlled and a voltage-controlled power circuit are used [40]. In [40], a model-based NSE was developed. The authors used two separate power sources: a controllable linear voltage regulator and a controllable linear current regulator. The voltage regulator is active when the operating points are along the MPP to the open-circuit point of the current–voltage (*I–V*) curve. In a complementary fashion, the current regulator is active when the operating points are along the MPP to the short-circuit point. For hot-swapping operation (i.e., continuous transition from using one active power source to the other) when the operating points are close to the MPP, the two power sources are connected with two parallel diodes in order to block the reverse current that may flow from one power source to the other.

In all these three categories, the reference generator can be realized by either an analog or digital circuit. An analog circuit can be based on diode or transistor p-n junction [1], [30], [31], or real photodiode illuminated by external light source [29], [32], [33]. A digital circuit can have a core of either a lookup table containing information of *I–V* curve or a mathematical program that calculates and interpolates the output reference based on its inputs [40]–[42].

Table I summarizes the characteristics of the existing NSEs in terms of their dynamic performance to a load step, the availability of a load step between nominal and short circuit, a load step between nominal and open circuit, and an input source step change.

D. Open Challenges

Despite the abundant availability of different existing NSEs, none of them qualifies for nonterrestrial applications. First, all of the important tests namely the load step between nominal and short-circuit test, the load step between nominal and open-circuit test, and the step change of the input source such as wind, fuel, or irradiation are missing. Most importantly, the existing NSEs are not sufficiently fast to closely resemble real PV arrays. As mentioned in Section I-B, a worst settling time of tens of microseconds is expected under a load step. However, as Table I has shown, the fastest among the existing NSEs needs 3.2 ms [39] to settle, which is a factor of several hundred times slower than the desired tens-of-microsecond response. It can be said that there is an enormous gap from the dynamic performance of existing PV emulators to that of real PV panels under extreme conditions.

E. Scope of This Paper

This paper seeks to address the aforementioned discrepancies in the research about NSEs. The design goal is to achieve a very high dynamic performance NSE that best resembles real PV panels under extreme test conditions. The transient response goal is 10 μs for the load switching operations as well as for the step change of input source. The proposed system, which consists of a nonisolated synchronous buck converter with a fourth-order output filter and an analog PV array small-signal generator (SSG) circuit, is investigated both theoretically and experimentally. The power rating of the proposed prototype is 200 W. The maximum output power can be changed by adjusting the parallel resistor and the short-circuit current reference in the SSG. The experimental results show the proposed NSE can achieve a 10-μs transient response with different test conditions. Moreover, the known prior works are at least 320 times slower, such as ([39], 3.2 ms), ([38], 3.6 ms), ([35], [36], 6 ms), ([37], 8 ms), and ([40], 100 ms). Compared to those works, the proposed converter is much faster as well as closer in resembling a real PV panel's electrical characteristic. It also offers a big advantage in the MPP tracking performance because MPP tracking algorithms would be possibly made faster without compromis-

TABLE I
SPECIFICATIONS AND CHARACTERISTICS OF EXISTING PV EMULATORS

Reference(s)	Step change of load settling time	Load step nom. to open	Load step nom. to short	Step change of input source	Power circuit
Koran 2010 [38]	3.8 ms ([38, Fig. 17])	No	No	No	buck with *LCLC* filter
Kim 2013 [40]	100 ms ([40, Fig. 15])	No	No	No	linear voltage and current regulators
Chang 2013 [35]	6 ms ([35, Fig. 12])	No	No	No	*LCLC* resonant dc–dc converter
Koran 2014 [39]	3.2 ms ([39, Fig. 15])	No	No	No	ac–dc three phase rectifier
Gadelovits 2014 [37]	8 ms ([37, Fig. 15])	No	No	No	commercial power supply
Chang 2014 [36]	6 ms ([36, Fig. 14])	No	No	No	*LCLC* resonant dc–dc converter
[1], [29]–[34]	Not found	No	No	No	linear power stage

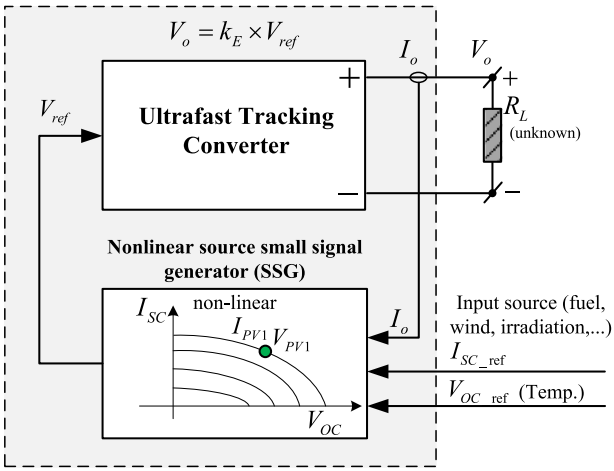

Fig. 9. Proposed system configuration.

ing the dynamic of the proposed NSE if it were used. From a broader perspective, together with its state-of-the-art dynamic performance, the proposed emulator with proper adjustment will also be able to emulate any slower nonlinear sources such as fuel cell and battery, or PV arrays working in terrestrial applications that focus on MPP tracking.

The structure of this paper is as follows. Section I is dedicated to the introduction. Following that, Section II will discuss the proposed NSE, its control approach, and circuitry. Section III will present the experimental results. Section IV will be a summary and conclusion of the work.

II. PROPOSED NSE

A. Proposed System Schematic

The proposed system configuration is shown in Fig. 9. The system consists of a voltage-controlled ultrafast tracking converter (VCTC) and a PV array SSG. The proposed system falls into the first category mentioned in Section I-C. In the proposed NSE, the output of the VCTC represents the output of the emulated PV array. The output current is sensed and fed to the SSG. Inside the SSG, the short-circuit current and the open-circuit voltage can be adjusted. The SSG generates the voltage reference for the ultrafast tracking converter. In this figure, k_E is the dc gain of the VCTC.

In relation to the system configuration shown in Fig. 9, the detailed schematic of the proposed NSE is shown in Fig. 10. In this circuit, the steady-state operation and the gradient of the current–voltage (*I–V*) curve is determined by three parameters. The short-circuit current is determined by the value of $I_{\rm SC}$; in this prototype, $I_{\rm SC}$ is converted to a voltage signal, $V_{I_{\rm SC}}$, with (1 V/1 A) conversion. Therefore, $I_{\rm SC}$ can be externally programmed by applying a voltage signal $V_{I_{\rm SC}}$ corresponding to it. The parallel resistor, which determines the gradient (or the slope) of the *I–V* curve around the constant current region, is represented by R_P. The open-circuit voltage is controlled by k_E, k_V, and R_I. Changing one among these three variables will change the open-circuit voltage of the proposed NSE.

The output current I_o is sensed by a precision current sensed resistor of 0.1 Ω in series with the output load R_L. The voltage drop across the sensed resistor is scaled by a factor of 10 to attain a conversion of 1 V/1 A. The output voltage V_o and the voltage across capacitor V_{C_1} are taken directly to the controller consisting of operational amplifier OA1 and their feedback impedances without any buffering or prescaling circuits.

The SSG in the bottom of Fig. 10 consists of summation circuits, a voltage to current (V2I) converter, and a diode circuit. The V2I consists of p-n-p transistors and operational amplifier OA2. V_{CC} is the 12 V control supply for all the operational and differential amplifiers. The negative control supply, $-V_{CC} = -12$ V, is applied to the cathode of diode D in order to ensure that the V2I converter can operate properly. As can be seen from the five-parameter model shown in Fig. 4, the current flows through the diode is equal to the difference between the short-circuit current $I_{\rm SC}$ and the output current I_o. Using the proposed SSG circuit shown in Fig. 10, the voltage signal that is the difference between $I_{\rm SC}$ and I_o (in volt) is converted to current I_D (in ampere) by

$$I_D = \frac{V_{I_{\rm SC}} - V_{I_o}}{R_I}(\text{A}). \tag{6}$$

Thus, the voltage-drop across diode D and R_P will be the signal-level NSE output voltage. A single differential amplifier

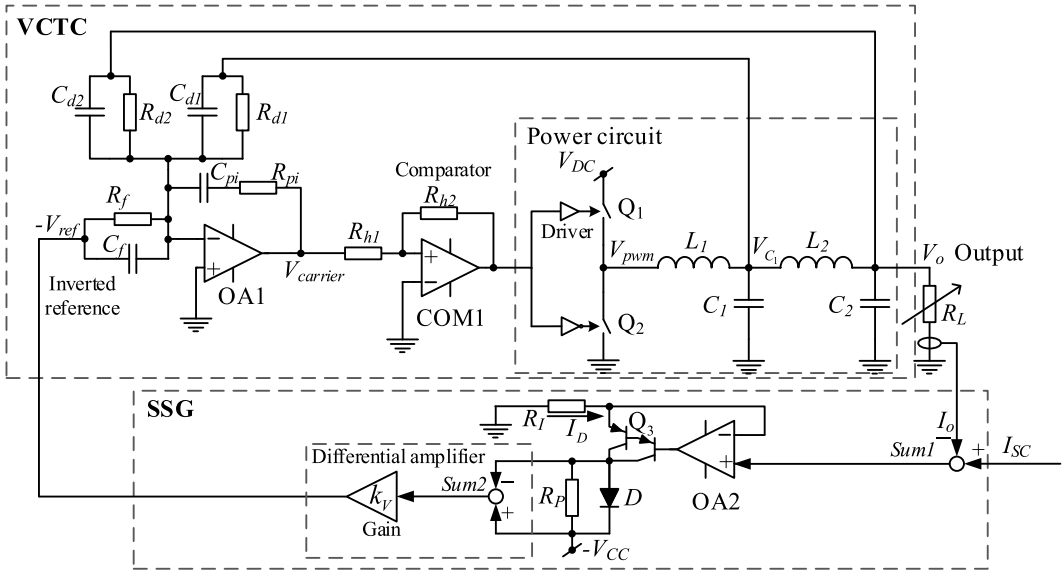

Fig. 10. Schematic of the proposed NSE.

circuit takes the voltage across D by a summation function denoted by *Sum2* and scales it with a positive gain k_V. Notice the polarity of the summation function *Sum2* in Fig. 10. The resulting voltage, $-V_{\rm ref}$, will be the inverted reference voltage for the VCTC.

The reason for the reference voltage fed to OA1 to be its inverted signal is because it is connected to the inverting input of OA1, which will be then inverted in polarity once again at OA1's output. At the same time, the output voltage V_o and the voltage across the first output filter capacitor V_{C_1} are fed directly to the inverting input of OA1 through their feedback impedance consisting of (R_{d2}, C_{d2}) and (R_{d1}, C_{d1}), respectively. Doing so, the original reference voltage signal will appear at the output of OA1, while the feedback signals will appear with their inverted polarity. The conditioning gains for the feedback signals are primarily determined by the ratios of feedback resistors to R_f, which are (R_{d2}/R_f) for V_o and (R_{d1}/R_f) for V_{C_1}. All of these can be explained further in the modeling of the control system that will be presented later in the next section.

It must be noted that the output voltage of a nonlinear source such as a battery source, a PV panel, or a fuel cell system is usually ripple-free; therefore, the output of a high-performance NSE should produce a ripple that is as low as possible. For this reason, a fourth-order output filter is utilized at the output of the tracking converter instead of a second-order output filter because of its possible higher attenuation, given that the same switching frequency is used. The output filter transfer function, which is from the pulse power signal, $V_{\rm pwm}$, to the output voltage V_o is approximated at high frequency by

$$G_{\rm FLT}(s)_{(s\gg\max(j\omega_1,j\omega_2))} = \frac{V_o(s)}{V_{\rm pwm}(s)}_{(s\gg\max(j\omega_1,j\omega_2))} \approx \frac{1}{s^4 L_1 L_2 C_1 C_2} = \frac{\omega_1^2\omega_2^2}{s^4} \tag{7}$$

TABLE II
PARAMETERS OF THE TRACKING CONVERTER AND ITS CONTROL

L_1	3.3 μH	C_f	1 nF
L_2	3.3 μH	R_{d1}	20 kΩ
C_1	100 nF	C_{d1}	47 pF
C_2	1360 nF	R_{d2}	20 kΩ
$V_{\rm DC}$	60 V	C_{d2}	470 pF
R_{h1}	6.2 kΩ	R_{pi}	1 kΩ
R_{h2}	51 kΩ	C_{pi}	470 pF
R_f	1 kΩ	$V_{\rm CMP}$	5 V
k_E	10		

where $\omega_1 = \frac{1}{\sqrt{L_1 C_1}}$ and $\omega_2 = \frac{1}{\sqrt{L_2 C_2}}$ are the natural frequency of each filter stage.

At the switching frequency ω_{sw} (rad/s), the magnitude of the output filter is

$$|G_{FLT}(j\omega_{sw})| \approx \frac{\omega_1^2\omega_2^2}{\omega_{sw}^4}. \tag{8}$$

With the filter value provided in Table II and with a switching frequency of 1 MHz, from (8), the fundamental harmonic at the output of the tracking converter will have a magnitude of approximately 35 mV peak to peak.

It needs to be paid attention to that a hysteresis self-oscillating modulated system as in this case suffers from a variable switching frequency. The switching frequency profile varies along a parabolic curve with regard to the change of duty cycle, where its maximum is at the duty cycle of 0.5 and it reduces quickly when the duty cycle is moving toward either zero or unity [43]–[46]. As (8) has shown, if the switching frequency becomes lower, the output ripple will become higher, which is not desirable. It is suggested that the switching frequency be kept constant regardless of the duty cycle so that a small ripple is always achieved. One of the approaches is to adjust the

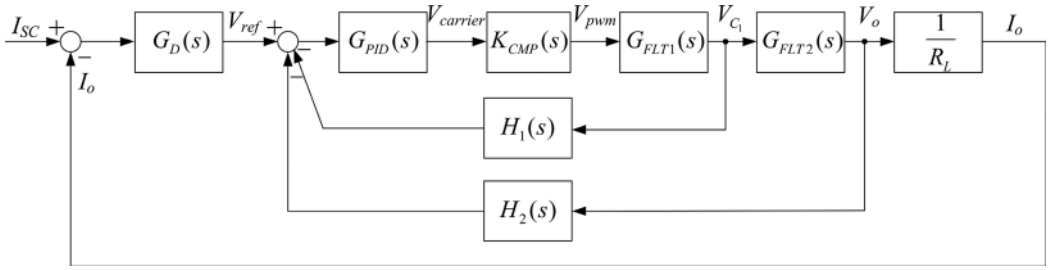

Fig. 11. Block diagram of the control system.

hysteresis threshold dynamically in a closed loop, such as in [43] and [45]. In that approach, the pulse width modulation (PWM) signal frequency is converted to a voltage signal by means of a frequency to voltage converter. The feedback frequency is compared to the reference frequency and the error is processed by a compensator. The output of the compensator adjusts the hysteresis threshold so that the switching frequency converges to the reference frequency. Another approach is to take the output of that compensator and inject it as an absolute gain into the loop that contains the hysteresis modulator, such as in [46]. The practical issue of variable switching frequency inherent in a hysteresis self-oscillating modulated system, however, is not addressed in this paper, which focuses on fast dynamic responses under different load steps and step change of input source. In a similar manner, the design of a power supply that is highly immune to the high *dv/dt* at the output of the NSE can be found in [47]–[50]. Other references relevant to this paper can be found in [54]–[63].

B. Control System Modeling

The block diagram of the control system is shown in Fig. 11. The modeling of the proposed control system is as follows. $G_D(s)$ is the transfer function from the difference between the short-circuit current $I_{\rm SC}$ and the output current I_o to the reference voltage $V_{\rm ref}$

$$G_D(s) = \frac{k_V Z_D R_P}{R_I(Z_D + R_P)} \tag{9}$$

where Z_D is the impedance of the diode D used. The transfer function of the proportional-integral-derivative (PID) controller as shown is

$$G_{\rm PID}(s) = \frac{(R_{pi}C_{pi}s+1)(R_f C_f s+1)}{C_{pi}R_f s}. \tag{10}$$

$K_{\rm CMP}(s)$ is the transfer function from the output of the PID controller to the pulse power signal $V_{\rm pwm}$. A detail treatment of $K_{\rm CMP}(s)$ can be found in, for example, [51, page 2-4]. Works [45], [52] approximated $K_{\rm CMP}(s)$ to be an infinite gain and achieved reasonable results. For simplicity, in this work, $K_{\rm CMP}$ is simplified to be a dc gain which is

$$K_{\rm CMP}(s) = \frac{V_{\rm pwm}(s)}{V_{\rm carrier}(s)} \approx \frac{V_{\rm DC}}{\varepsilon} = \frac{V_{\rm DC}R_{h2}}{V_{\rm CMP}R_{h1}} \tag{11}$$

where $\varepsilon = \frac{V_{\rm CMP}R_{h1}}{R_{h2}}$ is the hysteresis threshold and $V_{\rm CMP}$ is the output of the comparator COM1.

$G_{\rm FLT1}(s)$ is the transfer function from $V_{\rm pwm}$ to V_{C_1}, which is (by [45])

$$G_{\rm FLT1}(s) = \frac{V_{C_1}(s)}{V_{\rm pwm}(s)} = \frac{s^2L_2C_2 + sL_2/R_L + 1}{den(s)} \tag{12}$$

where the denominator $den(s)$ is equal to

$$\begin{aligned} den(s) &= s^4L_1L_2C_1C_2 + s^3L_1L_2C_1/R_L \\ &\quad + s^2(L_1C_2 + L_1C_1 + L_2C_2) + s(L_1+L_2)/R_L + 1. \end{aligned} \tag{13}$$

$G_{\rm FLT2}(s)$ is the transfer function from V_{C_1} to V_o, which is

$$G_{\rm FLT2}(s) = \frac{V_o(s)}{V_{C_1}(s)} = \frac{1}{s^2L_2C_2 + sL_2/R_L + 1}. \tag{14}$$

The most inner feedback transfer function is

$$H_1(s) = \frac{R_f(R_{d1}C_{d1}s+1)}{R_{d1}(R_fC_fs+1)}. \tag{15}$$

Likewise, the output-voltage feedback transfer function is

$$H_2(s) = \frac{R_f(R_{d2}C_{d2}s+1)}{R_{d2}(R_fC_fs+1)}. \tag{16}$$

The most inner loop closed-loop transfer function is

$$\begin{aligned} G_{\rm IN-CL}(s) &= \frac{V_{C_1}(s)}{V_{\rm ref}(s) - V_o(s)H_2(s)} \\ &= \frac{G_{\rm PID}(s)K_{\rm CMP}(s)G_{\rm FLT1}(s)}{1 + G_{\rm PID}(s)K_{\rm CMP}(s)G_{\rm FLT1}(s)H_1(s)}. \end{aligned} \tag{17}$$

Since $K_{\rm CMP}(s)$ is a very high gain, $G_{\rm IN\text{-}CL}(s)$ can be approximated to be

$$G_{\rm IN\text{-}CL}(s) \approx \frac{1}{H_1(s)}. \tag{18}$$

The transfer function from the reference voltage to the output voltage is then

$$G_V(s) = \frac{V_o(s)}{V_{\rm ref}(s)} = \frac{G_{\rm IN\text{-}CL}(s)G_{\rm FLT2}(s)}{1 + G_{\rm IN\text{-}CL}(s)G_{\rm FLT2}(s)H_2(s)} \tag{19}$$

$$\approx \frac{G_{\rm FLT2}(s)}{H_1(s) + G_{\rm FLT2}(s)H_2(s)}. \tag{20}$$

A Bode plot of $G_V(s)$ based on (19) and the parameters in Table II is shown in Fig. 12 for different loads.

Fig. 13 shows the transfer function from $V_{\rm ref}(s)$ to $I_o(s)$ at 47-Ω load measured with the Bode 100 Analyzer. This transfer function is equal to the closed-loop transfer function from

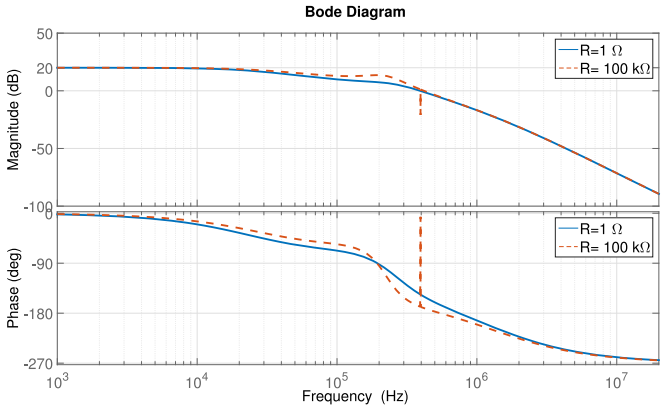

Fig. 12. Bode plot of the closed voltage loop $G_V(s)$ at different loads.

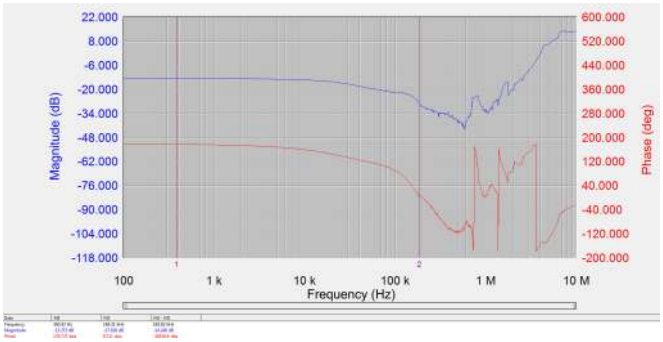

Fig. 13. Measured Bode plot of the transfer function from $V_{\rm ref}(s)$ to $I_o(s)$ at 47-Ω load.

$V_{\rm ref}(s)$ to $V_o(s)$ divided by a load of 47 Ω, or 33.4 dBΩ. Therefore, the dc gain of the measurement (the blue curve) is 20 dB − 33.4 dB = −13.4 dB. The phase shown in the red curve is measured in closed loop, so it is equal to the phase of the transfer function from $V_{\rm ref}(s)$ to $V_o(s)$ plus 180°. It can be seen the shape and value of the gain and phase correspond well with those in the model of Fig. 12, except for the high-frequency region where sampling effects at the switching frequency and above occur.

With the circuit schematic shown in Fig. 10, the amplification factor k_E of the closed-loop tracking converter shown in Fig. 9 will have the following formula:

$$k_E = G_V(0) = \frac{R_{d1}R_{d2}}{R_f(R_{d1}+R_{d2})}. \tag{21}$$

From the resistance values in Table II, k_E is equal to 10. Thus, 1 V of the reference voltage $V_{\rm ref}$ will produce 10 V of the output voltage V_o.

III. Experimental Results

The experimental studies have examined the proposed NSE under three typical operating conditions usually faced in nonterrestrial applications. They are the steady-state response along the static *I–V* curve, the series switching regulator tests, and the step change of input source. In addition, the fourth test is also added, that is a *fictitious* step change of temperature. The fourth test is fictitious because a step change of temperature is physically unrealizable because of the thermal inertia of the PV material. After a sudden change of input source, a PV panel will usually take approximately 30 min to reach its steady-state temperature [53]. Although a step change of temperature is unlikely, the test will still be carried out here in this work in order to verify the dynamic capability of the proposed NSE.

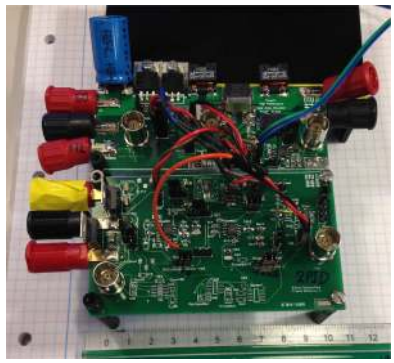

Fig. 14. Photo of the prototype.

The proposed circuit, unfortunately, suffers from instability at short-circuit current. According to [40], this is an intrinsic characteristic of the voltage-control approach. Also, according to [40], the current control approach does not have similar problem in the short-circuit region, but it suffers from poor controllability and stability near the open-circuit region.

The instability of the proposed NSE at operating points close to the short circuit can be explained as follows. Near the short-circuit region of the *I–V* curve, the load impedance R_L is small in Ohmic value, making the gain from V_o to I_o become large compared to that in other region. In addition, the output current is approaching $I_{\rm SC}$, which will make I_D approach zero. This small current makes the impedance of diode D approach infinitive according to the diode *I–V* curve. This makes $G_D(s)$ becomes very large. The open-loop gain that consists of $G_D(s), G_V(s)$, and $\frac{1}{R_L}$ becomes also very large. Its crossover frequency will move toward higher frequency, where the phase margin becomes negative (see Fig. 12), which in turn causes the system instability.

The load step between nominal and short-circuit problem of voltage-controlled NSE will not be addressed in this paper; it may the treated in a separate future work.

A photo of the prototype can be found in Fig. 14. The prototype has a dimension of 10 cm×10 cm. The upper part is the power circuit, which is the synchronous buck converter with a two-stage LC output filter plus a heat sink. The lower part contains all the feedback and control circuitry.

A. Steady-State Response

Figs. 15 and 16 show the steady-state current–voltage (*I–V*) and power–voltage (*P–V*) curves generated by the prototype with the set up in Table III. The short-circuit current is programmed to be 5 A by inputting a voltage $V_{I_{\rm SC}}$ of 5 V. When the load is open, there will be no output current and therefore, V_{I_o} is equal to zero. According to (6), a forward current of 0.33 A will

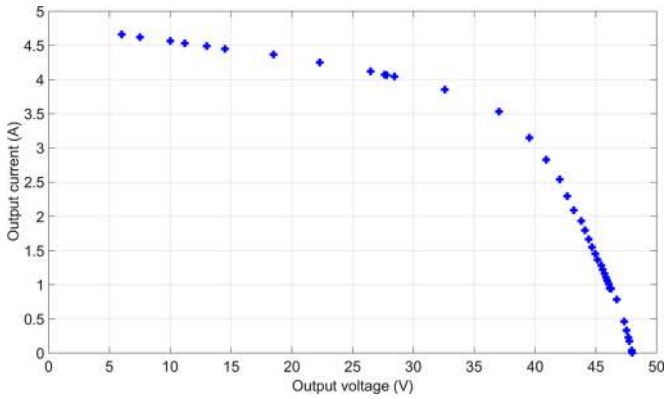

Fig. 15. Static current–voltage (*I–V*) curve generated by the proposed NSE.

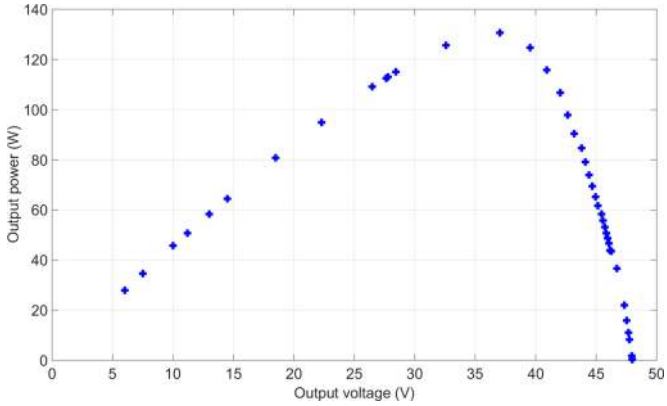

Fig. 16. Static power–voltage (*P–V*) curve generated by the proposed NSE.

TABLE III
PARAMETERS USED TO GENERATE STATIC *I–V* CURVE

Parameter	Value
I_{SC}	5 A
R_P	10 Ω
R_I	15 Ω
k_V	5
V_{OC}	48 V

flow through diode D. This develops a diode forward voltage drop of approximately 0.96 V. With the gain factor k_V of the differential amplifier equal to 5, this gives a voltage reference V_{ref} of approximately 4.8 V. This results in an open-circuit voltage of 48 V because k_E is equal to 10 by design.

As can be seen, the output voltage and current resemble the output of a PV panel. The MPP with this set up is 131 W at a load impedance of approximately 10 Ω.

B. Series Switching Regulation

Fig. 17 shows the transient responses of the proposed NSE under a series-type switching regulation. The load is switching between two values: open circuit (where the load is infinitive) and a fixed load. The switching frequency of the load is about

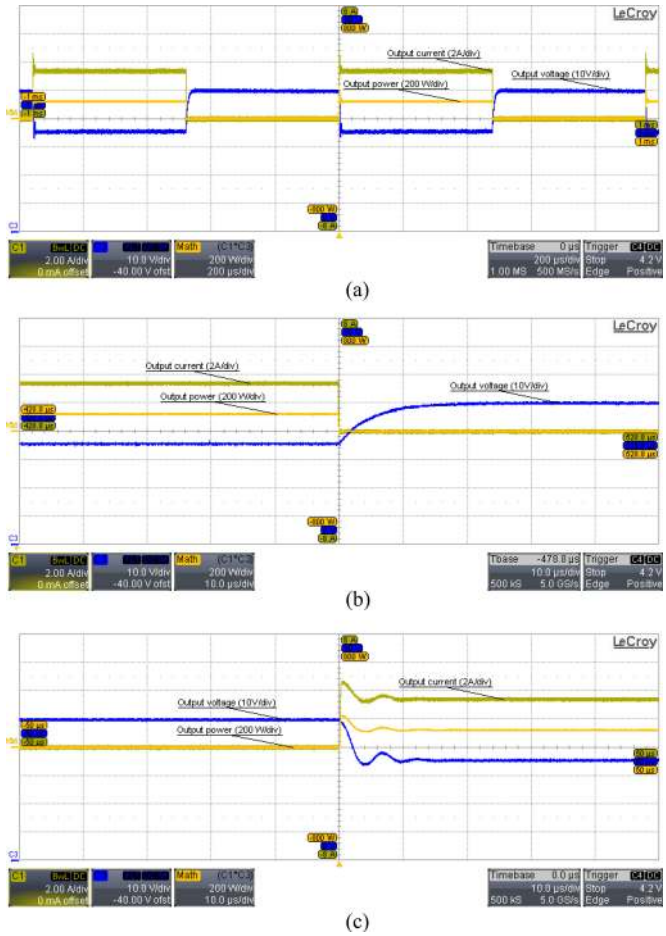

Fig. 17. Series load step test (a) switching transient between a nominal load and open circuit (b) partial zoom of the circuit transients from nominal load to open circuit (c) partial zoom of the circuit transients from open circuit to nominal load. Channel 1 (olive color): output current, 2 A/div. Channel 3 (blue color): output voltage, 10 V/div. Channel Math (C1*C3) (orange color): output power, 200 W/div. Time scale: 200 μs/div, 10 μs/div, and 10 μs/div, respectively.

1 kHz. As can be seen, the output voltage and current finish each transient within 10 μs. It is interesting to observe the experimental *I–V* curve of this test recorded directly from the oscilloscope used in the tests, which can be referred to Fig. 18(a). Meanwhile, Fig. 18(b) explains the process of Fig. 18(a), which will be as follows. The NSE is switching between denoted operating points A and B of Fig. 18(b). Right after the fixed load is inserted to the output of NSE, the circuit immediately moves from operating point A to interim point A1. During this period, the voltage does not change yet due to its disturbance rejection capability, while the new current value will be the result of the voltage at operating point A divided by the fixed load. After that, the regulation of the NSE makes the circuit move from A1 to operating point B, and the whole process from A to B takes only 10 μs [see Fig. 17(c)]. From that moment, the circuit settles at B until the load experiences a new step change. Likewise, when the load is switched from the fixed load to open circuit, which enforces a transient from operating point B to A, the operating point will first and immediately move from B to interim point B1. Following that, it will move from B1 to A and settle at A.

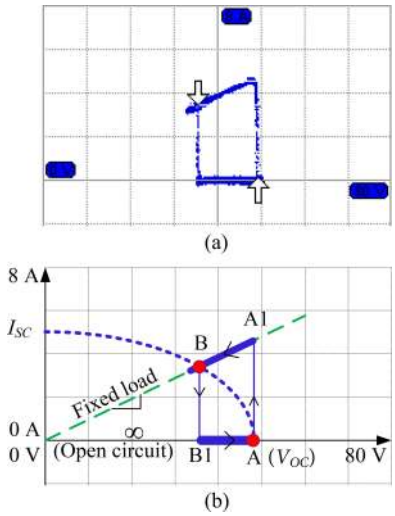

Fig. 18. Series test. (a) Experimental *I–V* curve and (b) its analytical waveform.

The whole transition from B to A also takes only 10 μs, which can be verified from Fig. 17(b).

The two arrows in Fig. 18(a) are originated from two cursors of the oscilloscope. They show the location of the operating point (A and B) in Fig. 18, but they are not visible from Fig. 17.

C. Step Change of Input Source

The results of the step change of input source are shown in Figs. 19 and 20. In Fig. 19, channel 2 (red color) is the short-circuit current I_{SC}. The input source change causes a change of short-circuit current from 2 to 5 A and *vice versa*. From Fig. 19(b) and (c), the circuit only takes 10 μs to complete the transition. The experimental *I–V* curve is shown in Fig. 20(a) and its behavior is explained in Fig. 20(b). A reduction of input source level from 5 to 2 A short-circuit current will make the NSE move from point A to B, and an increase of input source in the other direction will make the NSE move from point B to A. Each transition takes only 10 μs.

D. Dynamic Change of Temperature

As discussed in Section II-A, the open-circuit voltage is determined by k_E, k_V, and R_I. Furthermore, the open-circuit voltage is mainly determined by the temperature. Therefore, changing the open-circuit voltage by means of adjusting one of the three parameters k_E, k_V, and R_I will give the same effect as changing temperature.

The fictitious step change of temperature can be simulated by performing a step change between different values of R_I. To demonstrate this, the value of R_I is switched back and forward between 15 and 30 Ω. The results are shown in Figs. 21 and 22. The short-circuit current is fixed at 5 A. When changing the temperature, the short-circuit current does not change, but the profile of *I–V* curve changes as shown in Fig. 22(b). As can be seen from these results, under a step change of temperature, the proposed NSE only takes about 10 μs to complete a transition.

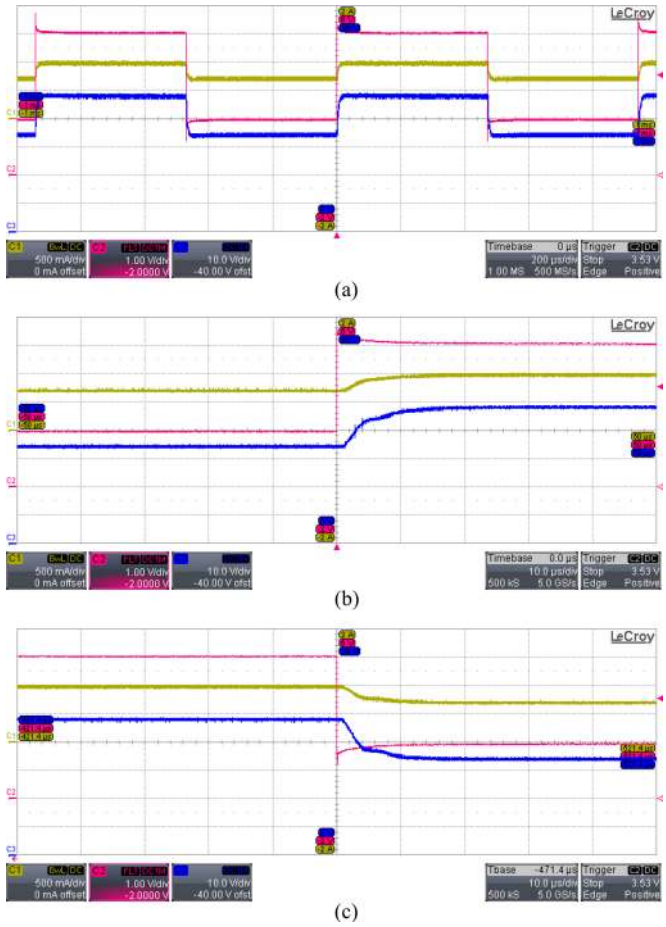

Fig. 19. Emulation of input source step change (a) switching transient between two input source levels (b) partial zoom of the transients from a low to high input source level (c) partial zoom of the transients from a high to low input source level. Channel 1 (olive color): output current, 2 A/div. Channel 3 (blue color): output voltage, 10 V/div. Channel 2 (red color): input source level, 1 A/div. Time scale: 200 μs/div, 10 μs/div, and 10 μs/div, respectively.

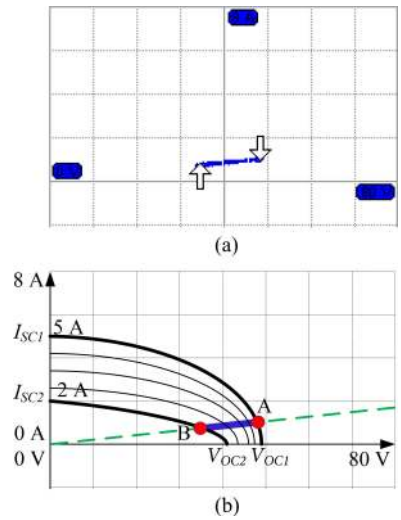

Fig. 20. Step change of input source. (a) Experimental *I–V* curve and (b) its analytical waveform.

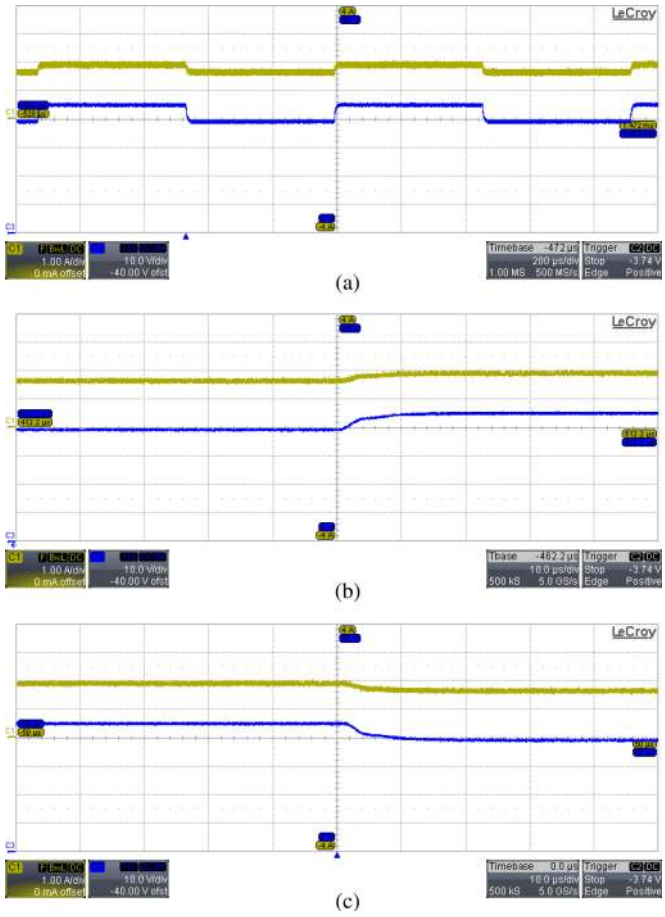

Fig. 21. Emulation of fictitious temperature step change (a) switching transient between two temperature levels (b) partial zoom of the transients from a low to high temperature level (c) partial zoom of the transients from a high to low temperature level. Channel 1 (olive color): output current, 1 A/div. Channel 3 (blue color): output voltage, 10 V/div. Time scale: 200 μs/div, 10 μs/div, and 10 μs/div, respectively.

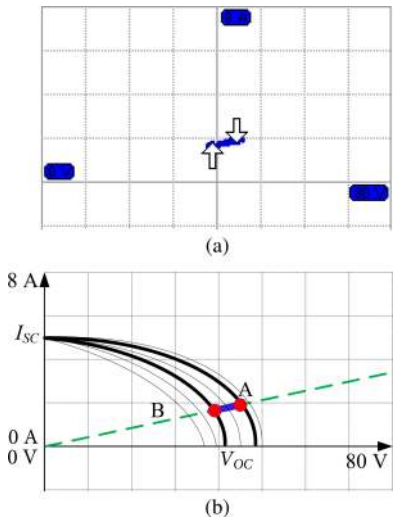

Fig. 22. Fictitious temperature step change effect. (a) Experimental *I–V* curve and (b) its analytical waveform.

IV. Conclusion

This paper has proposed and demonstrated an NSE system with high dynamic performance. The result that has been achieved is a 200-W NSE capable of simulating series-type switching tests and step change of input source tests with the fastest transient response ever reported, 10 μs. This work, therefore, has provided a state-of-the-art solution for simulating different nonlinear sources in nonterrestrial as well as terrestrial applications.

The presence of the intrinsic source capacitance in a real PV system determines its transient response under a load step. This quantity should be taken into account in the design of the PV emulator. In addition, the output of a nonlinear source usually does not contain ripple. Therefore, it is desired that the developed NSE's output ripple to be as low as possible. This can be achieved by high order filtering of the NSE. The switching frequency drop that is inherent in a hysteresis self-oscillating controlled system needs to be paid attention because it increases the output voltage ripple.

It must be acknowledged, however, that the proposed method contains several limitations. The first issue is the stability when the NSE operates in the short-circuit region. One approach is to design a more robust control structure, which raises open issues for future study. Another approach is to use a dual-mode power circuit that consists of a separate voltage source and a separate current source power circuit. Deactivating the voltage source and activating the current source power circuit when the NSE operates in the short-circuit region may solve the problem. The second issue is to solve the load step between nominal and short circuit. Once the stability issue in the short-circuit region is solved, this issue may get easier to be tackled.

Finally, for future work, it might be beneficial to realize the nonlinear curve small-signal reference generator by means of an advanced digital control unit, such as high-speed FPGA, in order to take into account multiple parameter changes at the same time or to allow for more flexible setting of test conditions.

Acknowledgment

The authors would like to thank the reviewers for their constructive comments, which greatly improved the revised manuscript.

References

[1] D. Schofield, M. Foster, and D. Stone, "Low-cost solar emulator for evaluation of maximum power point tracking methods," *Electron. Lett.*, vol. 47, no. 3, pp. 208–209, Feb. 2011.

[2] C. Park, J. Liu, and P. Chou, "B#: A battery emulator and power-profiling instrument," *IEEE Design Test Comput.*, vol. 22, no. 2, pp. 150–159, Mar. 2005.

[3] P. Chou, C. Park, J. Park, K. Pham, and J. Liu, "B#: A battery emulator and power profiling instrument," in *Proc. Int. Symp. Low Power Electron. Design*, Aug. 2003, pp. 288–293.

[4] O. Konig, S. Jakubek, and G. Prochart, "Model predictive control of a battery emulator for testing of hybrid and electric powertrains," in *Proc. IEEE Veh. Power Propulsion Conf.*, Sep. 2011, pp. 1–6.

[5] O. Konig, S. Jakubek, and G. Prochart, "Battery impedance emulation for hybrid and electric powertrain testing," in *Proc. IEEE Veh. Power Propulsion Conf.*, Oct. 2012, pp. 627–632.

[6] O. Konig, C. Hametner, G. Prochart, and S. Jakubek, "Battery emulation for power-hil using local model networks and robust impedance control," *IEEE Trans. Ind. Electron.*, vol. 61, no. 2, pp. 943–955, Feb. 2014.

[7] T. Mesbahi, N. Rizoug, P. Bartholomeus, and P. Le Moigne, "Li-ion battery emulator for electric vehicle applications," in *Proc. IEEE Veh. Power Propulsion Conf.*, Oct. 2013, pp. 1–8.

[8] A. Thanheiser, T. Kohler, C. Bertram, and H. Herzog, "Battery emulation considering thermal behavior," in *Proc. IEEE Veh. Power Propulsion Conf.*, Sep. 2011, pp. 1–5.

[9] J. Correa, F. Farret, J. Gomes, and M. Simoes, "Simulation of fuel-cell stacks using a computer-controlled power rectifier with the purposes of actual high-power injection applications," *IEEE Trans. Ind. Appl.*, vol. 39, no. 4, pp. 1136–1142, Jul. 2003.

[10] M. Ordonez, M. Iqbal, and J. Quaicoe, "Development of a fuel cell simulator based on an experimentally derived model," in *Proc. Canadian Conf. Electr. Comput. Eng*, May 2005, pp. 1449–1452.

[11] J.-G. Lim, S.-H. Kim, E.-K. Seo, H.-B. Shin, S.-K. Chung, and H. woo Lee, "Implementation of fuel cell dynamic simulator," in *Proc. 37th IEEE Power Electron. Spec. Conf.*, Jun. 2006, pp. 1–5.

[12] J.-G. Lim and S.-K. Chung, "Implementation of a fuel cell dynamic simulator," *J. Power Electron.*, vol. 7, no. 4, pp. 336–342, 2007.

[13] P. Acharya, P. Enjeti, and I. Pitel, "An advanced fuel cell simulator," in *Proc. 19th Annu. IEEE Appl. Power Electron. Conf. Expo.*, 2004, vol. 3, pp. 1554–1558.

[14] R. Kumar, M. Suresh, and J. Nagaraju, "Effect of solar array capacitance on the performance of switching shunt voltage regulator," *IEEE Trans. Power Electron.*, vol. 21, no. 2, pp. 543–548, Mar. 2006.

[15] J. Ibirriaga, X. de Mendiluce Pena, A. Opritescu, D. Sera, and R. Teodorescu, "Low-cost, high flexibility i-v curve tracer for photovoltaic modules," in *Proc. 12th Int. Conf. Optim. Electr. Electron. Equipment*, May 2010, pp. 1210–1215.

[16] D. S. H. Chan and J. C. H. Phang, "Analytical methods for the extraction of solar-cell single- and double-diode model parameters from i-v characteristics," *IEEE Trans. Electron Devices*, vol. ED-34, no. 2, pp. 286–293, Feb. 1987.

[17] K. Nguyen-Duy, A. Knott, and M. A. E. Andersen, "A review on the implementation of nonlinear source emulators," in *Proc. 55th Int. Sci. Conf. Power Electr. Eng. Riga Tech. Univ.*, Oct. 2014, pp. 56–62.

[18] C. Honsberg and S. Bowden. (2014, Nov.). Series resistance. [Online]. Available: http://www.pveducation.org/pvcdrom/solar-cell-operation/series-resistance

[19] T. Esram and P. Chapman, "Comparison of photovoltaic array maximum power point tracking techniques," *IEEE Trans. Energy Conver*, vol. 22, no. 2, pp. 439–449, Jun. 2007.

[20] G. J. Madden and A. Le, " Solar panel model for design and analysis of power regulation equipment," in *Proc. Intersoc. Energy Convers. Eng. Conf.*, 1994, vol. 1, pp. 151–156.

[21] J. M. Blanes, A. Garrigs, E. Sanchis, and J. A. Carrasco, " Modeling the sequential switching shunt series regulator," *IEEE Power Electron. Lett.*, vol. 3, no. 1, pp. 7–13, Mar. 2005.

[22] (2014, Feb.). Shunt-mode solar/wind charge controller. [Online]. Available: http://www.solorb.com/elect/solarcirc/shuntreg1/

[23] A. Patil, B. Cho, and F. Lee, "Design considerations for a solar array switching unit," in *Proc. 25th Intersoc. Energy Convers. Eng. Conf.*, Aug. 1990, vol. 1, pp. 373–379.

[24] B. H. Cho and D. H. Lee, *A Single PWM Section Solar Array Shunt Switching Unit with an Active Ripple Filter*. New York, NY, USA: ASME, Dec 1995.

[25] J. M. Blanes, A. Garrigs, E. Sanchis-Kilders, and J. A. Carrasco, "A new sequential switching shunt regulator—Digital shunt regulator (S3R-DSR) for solar array regulators," in *Proc. IEEE Int. Symp. Ind. Electron.*, 2006, vol. 2, pp. 1064–1069.

[26] A. Garrigos, J. Blanes, J. Carrasco, and J. Ejea, "Influence of the parasitic solar array capacitance in the sequential switching shunt series regulator," in *Proc. IEEE Mediterranean Electrotech. Conf.*, May 2006, pp. 1198–1201.

[27] K. E. Shum and C. R. Ashley, " A new full shunt switching unit for solar array using coupled-inductor boost converter," in *Proc. Intersoc. Energy Convers. Eng. Conf.*, 1996, vol. 1, pp. 617–622.

[28] K. Wu, " Loop gain of a spacecraft switched shunt power system," *IEEE Trans. Aerosp. Electron. Syst.*, vol. 30, no. 4, pp. 1049–1053, Oct. 1994.

[29] S. Armstrong, C. K. Lee, and W. Hurley, "Investigation of the harmonic response of a photovoltaic system with a solar emulator," in *Proc. Eur. Conf. Power Electron. Appl.*, 2005, p. 8.

[30] (2013, Dec.). Two bipolar transistors form a low-cost solar-array emulator. [Online]. Available: http://electronicdesign.com/energy/two-bipolar-transistors-form-low-cost-solar-array-emulator

[31] W. kui, L. Yongdong, R. Jianye, and S. Min, "Design and implementation of a solar array simulator," in *Proc. Int. Conf. Electr. Mach. Syst.*, Oct. 2008, pp. 2633–2636.

[32] H. Nagayoshi, "Characterization of the module/array simulator using i-v magnifier circuit of a pn photo-sensor," in *Proc. 3rd World Conf. Photovoltaic Energy Convers*, May 2003, vol. 2, pp. 2023–2026.

[33] H. Nagayoshi, "I–V curve simulation by multi-module simulator using I–V magnifier circuit," *Sol. Energy Materi. Sol. Cells*, vol. 82, no. 12, pp. 159–167, 2004.

[34] H. Nagayoshi and M. Atesh, "Partial shading effect emulation using multi small scale module simulator units," in *Proc. Conf. Rec. 31st IEEE Photovoltaic Spec. Conf.*, Jan. 2005, pp. 1710–1713.

[35] C.-H. Chang, E.-C. Chang, and H.-L. Cheng, "A high-efficiency solar array simulator implemented by an LLC resonant dc-dc converter," *IEEE Trans. Power Electron.*, vol. 28, no. 6, pp. 3039–3046, Jun. 2013.

[36] C. Chang, C. Cheng, and H. Cheng, "Modeling and design of the llc resonant converter used as a solar-array simulator," *IEEE J. Emerg. Sel. Topics Power Electron.*, vol. 2, no. 4, pp. 833–841, Dec. 2014.

[37] S. Gadelovits, M. Sitbon, and A. Kuperman, "Rapid prototyping of a low-cost solar array simulator using an off-the-shelf dc power supply," *IEEE Trans. Power Electron.*, vol. 29, no. 10, pp. 5278–5284, Oct. 2014.

[38] A. Koran, K. Sano, R. young Kim, and J.-S. Lai, "Design of a photovoltaic simulator with a novel reference signal generator and two-stage LC output filter," *IEEE Trans. Power Electron.*, vol. 25, no. 5, pp. 1331–1338, May 2010.

[39] A. Koran, T. LaBella, and J.-S. Lai, "High efficiency photovoltaic source simulator with fast response time for solar power conditioning systems evaluation," *IEEE Trans. Power Electron.*, vol. 29, no. 3, pp. 1285–1297, Mar. 2014.

[40] Y. Kim, W. Lee, M. Pedram, and N. Chang, "Dual-mode power regulator for photovoltaic module emulation," *Appl. Energy*, vol. 101, pp. 730–739, 2013.

[41] E. Koutroulis, K. Kalaitzakis, and V. Tzitzilonis, "Development of an FPGA-based system for real-time simulation of photovoltaic modules," in *Proc. 17th IEEE Int. Workshop Rapid Syst. Prototyping*, Jun. 2006, pp. 200–208.

[42] Y. Li, T. Lee, F. Peng, and D. Liu, "A hybrid control strategy for photovoltaic simulator," in *Proc. 24th Annu. IEEE Appl. Power Electron. Conf. Expo.*, Feb. 2009, pp. 899–903.

[43] D. Grant, "Frequency control of hysteretic power converter by adjusting hystersis levels," U.S. Patent 6 348 780, Feb. 19, 2002.

[44] S. Poulsen and M. Andersen, "Hysteresis controller with constant switching frequency," *IEEE Trans. Consum. Electron.*, vol. 51, no. 2, pp. 688–693, May 2005.

[45] M. Hoyerby and M. A. E. Andersen, "Ultrafast tracking power supply with fourth-order output filter and fixed-frequency hysteretic control," *IEEE Trans. Power Electron.*, vol. 23, no. 5, pp. 2387–2398, Sep. 2008.

[46] K. Nguyen-Duy, A. Knott, and M. Andersen, "Constant switching frequency self-oscillating controlled class-d amplifiers," *Elektronika ir Elektrotechnika*, vol. 20, no. 6, pp. 84–88, 2014.

[47] K. Nguyen-Duy, L. Petersen, A. Knott, O. Thomsen, and M. Andersen, "Design of a 300-watt isolated power supply with minimized circuit input-to-output parasitic capacitance," in *Proc. 7th IET Int. Conf. Power Electron., Mach. Drives*, Apr. 2014, pp. 1–6.

[48] K. Nguyen-Duy, Z. Ouyang, L. Petersen, A. Knott, O. Thomsen, and M. Andersen, "Design of a 300-watt isolated power supply for ultrafast tracking converters," *IEEE Trans. Power Electron.*, vol. 30, no. 6, pp. 3319–3333, Jun. 2015.

[49] K. Nguyen-Duy, Z. Ouyang, A. Knott, and M. Andersen, "Minimization of the transformer inter-winding parasitic capacitance for modular stacking power supply applications," in *Proc. 16th Eur. Conf. Power Electron. Appl.*, Aug. 2014, pp. 1–10.

[50] K. Nguyen-Duy, A. Knott, and M. Andersen, "Loss performance analysis of an isolated power supply for ultrafast tracking converters," in *Proc. IEEE Int. Power Electron. Appl. Conf. Expo.*, Nov. 2014, pp. 1543–1548.

[51] M. C. W. Høyerby and M. A. E. Andersen, "A small-signal model of the hysteretic comparator in linear-carrier self-oscillating switch-mode controllers," in *Proc. Nordic Workshop Power Ind. Electron.*, pp. 2–4, 2006.

[52] M. Hoyerby and M. A. E. Andersen, "Optimized envelope tracking power supply for Tetra2 base station RF power amplifier," in *Proc. 23rd Annu. IEEE Appl. Power Electron. Conf. Expo.*, Feb. 2008, pp. 777–783.

[53] (2014, Nov.). MPP Solar Tracker: The effect of module temperature and insolation. [Online]. Available: http://hespv.ca/hesproductspecs/technical-bulletins/fronius/SE_TA_MPP_Solar_Tracker_Effect_Module_Temperature_Insolation_EN_320488_snapshot.pdf
[54] Z. Housheng and Z. Yanlei, "Research on a novel digital photovoltaic array simulator," in *Proc. Int. Conf. Intell. Comput. Technol. Autom.*, May 2010, vol. 2, pp. 1077–1080.
[55] R. Kumar, M. Suresh, and J. Nagaraju, "Measurement of ac parameters of gallium arsenide (GaAs/Ge) solar cell by impedance spectroscopy," *IEEE Trans. Electron Devices*, vol. 48, no. 9, pp. 2177–2179, Sep. 2001.
[56] R. A. Kumar, M. Suresh, and J. Nagaraju, "Measurement and comparison of AC parameters of silicon (BSR and BSFR) and gallium arsenide (GaAs/Ge) solar cells used in space applications," *Sol. Energy Mater. Sol. Cells*, vol. 60, no. 2, pp. 155–166, 2000.
[57] K.-D. Rasch and K. Roy, " Shunt and blocking diodes for protection of space solar arrays," in *Proc. Conf. Rec. IEEE Photovoltaic Spec. Conf.*, 1981, pp. 550–553.
[58] N. N. Goryashin and A. S. Sidorov, " Solar array regulator based on buck converter with sequential switched sections," in *Proc. Int. Conf. Young Spec. Micro/Nanotechnol. Electron Devices*, 2013, pp. 364–368.
[59] M. Mira, A. Knott, O. Thomsen, and M. Andersen, "Boost converter with combined control loop for a stand-alone photovoltaic battery charge system," in *Proc. IEEE 14th Workshop Control Model. Power Electron.*, Jun. 2013, pp. 1–8.
[60] M. Hoyerby and M. A. E. Andersen, "TEDS base-station power amplifier using low-noise envelope tracking power supply," *IEEE Trans. Microw. Theory Techn.*, vol. 57, no. 7, pp. 1687–1693, Jul. 2009.
[61] M. Hoyerby and M. Andersen, "Carrier distortion in hysteretic self-oscillating class-d audio power amplifiers: Analysis and optimization," *IEEE Trans. Power Electron.*, vol. 24, no. 3, pp. 714–729, Mar. 2009.
[62] M. Villalva, J. Gazoli, and E. Filho, "Comprehensive approach to modeling and simulation of photovoltaic arrays," *IEEE Trans. Power Electron.*, vol. 24, no. 5, pp. 1198–1208, May 2009.
[63] L. Nousiainen, J. Puukko, A. Maki, T. Messo, J. Huusari, J. Jokipii, J. Viinamaki, D. Lobera, S. Valkealahti, and T. Suntio, "Photovoltaic generator as an input source for power electronic converters," *IEEE Trans. Power Electron.*, vol. 28, no. 6, pp. 3028–3038, Jun. 2013.

Khiem Nguyen-Duy (S'09) was born in Hanoi, Vietnam, on June 29, 1986. He received the B.S. degree in electrical engineering from the Hanoi University of Science and Technology, Hanoi, Vietnam, in 2009, the M.Sc. degree in electrical engineering from the National Taiwan University of Science and Technology, Taipei, Taiwan, in 2011, and the Ph.D. degree in power electronics from the Technical University of Denmark, Kongens Lyngby, Denmark, in April 2015.

He was a Visiting Scholar with the Colorado Power Electronics Center, University of Colorado Boulder, Boulder, CO, USA, during Summer 2014. He is currently a Hardware Design Engineer developing different electrical ground supporting equipment for satellites and spacecraft at SSBV-Rovsing, Skovlunde, Denmark. His research interests include power electronics, motor drives, and the application of advanced control theories to these fields, especially in matrix converters and switch-mode power converters.

Arnold Knott (M'10) received the Diplom-Ingenieur (FH) degree from the University of Applied Sciences, Deggendorf, Germany, in 2004, and the Ph.D. degree from the Technical University of Denmark, Kongens Lyngby, Denmark, in 2010, working on a research project under the title "Improvement of out-of-band Behaviour in Switch-Mode Amplifiers and Power Supplies by their Modulation Topology."

From 2004 until 2009, he was with Harman/Becker Automotive Systems GmbH in Germany and USA, designing switch-mode audio power amplifiers and power supplies for automotive applications. From 2010 to 2013, he was an Assistant Professor at the Technical University of Denmark, where he has been an Associate Professor since 2013. His interests include switch-mode audio power amplifiers, power supplies, active and passive components, integrated circuit design, acoustics, radio frequency electronics, electromagnetic compatibility, and communication systems.

Michael A. E. Andersen (M'88) received the M.Sc.E.E. and Ph.D. degrees in power electronics from the Technical University of Denmark, Kongens Lyngby, Denmark, in 1987 and 1990, respectively.

He is currently a Professor of power electronics at the Technical University of Denmark, where since 2009, he has been the Deputy Head of the Department of Electrical Engineering. He is the author or coauthor of more than 200 publications. His research interests include switch-mode power supplies, piezoelectric transformers, power factor correction, and switch-mode audio power amplifiers.